Efficient block-sparse model-based algorithm for photoacoustic image reconstruction

Chen Zhang [a], Yuanyuan Wang [a,b,*], Jin Wang [a]

[a] Department of Electronic Engineering, Fudan University, Shanghai 200433, China
[b] Key Laboratory of Medical Imaging Computing and Computer Assisted Intervention (MICCAI) of Shanghai, Shanghai, China

ARTICLE INFO

ABSTRACT

The model-based algorithm for photoacoustic imaging (PAI) has been proved to be stable and accurate. However, its reconstruction is computationally burdensome which limits its application in the practical PAI. In this paper, we proposed a block-sparse discrete cosine transform (BS-DCT) model-based PAI reconstruction algorithm in order to improve the computational efficiency of the model-based PAI reconstruction. We adopted the discrete cosine transform (DCT) to eliminate the minor coefficients and reduce the data scale. A block-sparse based iterative method was proposed to accomplish the image reconstruction. Due to its block independent nature, we used the CPU-based parallel calculation implementation to accelerate the reconstruction. During the iterative reconstruction, the number of required iterations was reduced by adopting the fast-converging optimization Barzilai–Borwein method. The numerical simulations and in-vitro experiments were carried out. The results has shown that the reconstruction quality is equivalent to the state-of-the-art iterative algorithms. Our algorithm requires less number of iterations with a reduced data scale and significant acceleration through the parallel calculation implementation. In conclusion, the BS-DCT algorithm may be an effectively accelerated practical algorithm for the PAI reconstruction.

© 2015 Elsevier Ltd. All rights reserved.

1. Introduction

Photoacoustic imaging (PAI) is an emerging technique that combines the high contrast of pure optical methods with the high spatial resolution of ultrasound imaging [1–6]. The potential of photoacoustic to image biological tissues has been shown in a variety of imaging applications, from structural imaging [7–9] of tumor detection [10,11], ocular imaging [12] and vascular anatomy [13,14] to functional imaging of blood oxygenation [15] and molecular contrast agents [16].

The physical basis of the PAI is the photoacoustic effect, which converts absorbed optical energy into pressure via thermoelastic expansion [2]. In this paper, we focus on the computed-tomographic PAI. In this imaging mode, the PAI is performed by illuminating an optically absorbing object with short high-power laser pulses and the generated photoacoustic signals are detected by ultrasonic transducers placed in multiple positions. The goal of the PAI is to obtain an estimate of the optical absorption distribution within the object from the received photoacoustic signals. To accomplish this, an image reconstruction algorithm is required.

A variety of analytical image reconstructions have been developed. The filtered back-projection (FBP) algorithm is the most popular algorithm [17,18]. Reconstruction algorithms in the time domain [19,20] and frequency domain [21–23] have been proposed in various geometries. The de-convolution reconstruction algorithm proposed by Zhang et al. has specific advantage under the circumstance of limited-angle sampling and heterogeneous acoustic medium [24,25]. These analytical reconstruction algorithms have been widely used for the PAI reconstruction due to their implementation convenience. However, these algorithms generally assume an idealized transducer model and ignore the measurement noises. These drawbacks limit the applications of the analytical algorithms and impair their performance. To overcome the limitation, iterative image reconstruction algorithms are proposed.

The typical PA image reconstruction problem can be considered as a source reconstruction problem. We need to build up a model to describe the relationship between the received ultrasound signals and the optical absorption distribution to solve this problem. So they are also called the model-based algorithms. Most of them calculate iteratively to get the optical absorption image. Previous

* Corresponding author at: Department of Electronic Engineering, Fudan University, No.220, Handan Rd., Shanghai 200433, China. Tel.: +86 21 65643526; fax: +86 21 65643526.
E-mail address: yywang@fudan.edu.cn (Y. Wang).

works have used least-square QR (LSQR) based decomposition methods in obtaining accurate reconstruction image [26–29]. The compressed sensing (CS) has been involved into the PAI reconstruction [30–34]. Some parameters in the aspect of image processing are also employed to assist the image reconstruction. Some algorithms are proposed by using total variation (TV) minimization to the PAI image reconstruction [35–40]. These TV-based algorithms are reported to be stable and efficient under the sparse-view circumstance for the PAI reconstruction. The iterative algorithms are widely used in the PAI reconstruction for its high-quality performance. However, the computation cost and memory storage required for the PAI reconstruction are excessively burdensome in implementing these algorithms. Acceleration of iterative PAI reconstruction algorithms will facilitate algorithm development and many potential clinical applications [26,41–43].

The structured compressed sensing [44] that exhibit additional structure in the signal recovery problem has been received much attention in the last few years. The block-sparse model [45–47], in which the nonzero elements are appearing in blocks rather than being arbitrarily spread, has been used to solve many compressed sensing recovery problem. It has been proved that when the number of the nonzero elements is fixed, block-sparsity has a better recovery performance than conventional sparsity [48]. During the iteration, the block-sparse model updates the signals block by block and the blocks are independent with each other. This property can be used to implement a parallelization strategies for improving the computational efficiency.

In this paper, we propose a novel efficient iterative algorithm to accelerate the image reconstruction in the PAI. We calculate the discrete cosine transform (DCT) coefficients from the received signals to make the energy of the signals concentrated and choose the relatively significant DCT coefficients for reconstruction to scale down the dataset. We include the block-sparse minimization into the PAI reconstruction for the first time. The block-sparse reconstruction algorithm helps to improve the imaging quality with less information. Due to its block independent nature, this algorithm can be easily implemented for parallelization strategies to accelerate image reconstruction in practical modalities. Our numerical studies and *in-vitro* experiments confirm that the proposed method is able to accelerate effectively and the quality of the reconstruction can be kept in a high level as well.

The remainder of the paper is organized as follows. In Section 2, we briefly introduce the block-sparse model and the procedures of the block-sparse model-based image reconstruction. Numerical studies and experimental results are described in Sections 3 and 4. Finally, a brief discussion and summary of the proposed algorithm is provided in Section 5.

2. Method

2.1. Photoacoustic-theory

We focus on two-dimensional PAI in this paper. Photoacoustic signals are usually generated by excitation of tissue by an ultra-short laser pulse. The heat is subsequently converted into pressure waves, which propagate through tissue. Then these photoacoustic signals are detected by the ultrasound transducer at different positions in the scanning plane. Based on the assumption that the illumination is spatially uniform and the laser pulse is sufficiently short, the relationship between the detected acoustic signals and the laser absorption distribution can be written as

$$\nabla^2 p(\vec{r}, t) - \frac{1}{c^2}\frac{\partial^2 p(\vec{r}, t)}{\partial t^2} = -\frac{\mu}{C_p}u(\vec{r}) \cdot \frac{\partial I(t)}{\partial t} \tag{1}$$

where $p(\vec{r}, t)$ is the acoustic pressure measurements at the position $\vec{r}$ and the time t, c is the sound speed, C_p is the specific heat, μ is the

isobaric expansion coefficient, $I(t)$ is the temporal profile of the laser pulse and $u(\vec{r})$ is the laser absorption distribution. In our study and many photoacoustic tomography studies, a laser pulse is employed with a very short duration. Its duration is nano seconds. So here we made an approximation to treat the $I(t)$ as a Dirac-delta function.

With assumption that the sound speed remains the same, Eq. (1) can be solved as follows:

$$p(\vec{r}_0, t) = \frac{\mu}{4\pi C_p}\frac{\partial}{\partial t}\oiint_{|\vec{r}-\vec{r}_0|=ct}\frac{u(\vec{r})}{t}\mathrm{d}^2\vec{r} \tag{2}$$

where $\vec{r}_0$ is the position of the ultrasound transducer.

While the back-projection algorithms seek to invert Eq. (2) analytically, the iterative model-based algorithms numerically invert a discretized version of Eq. (2). In model-based image reconstructions, a projection matrix A is typically established to connect the acoustic pressure measurements with the reconstructed image. The measurements can be calculated based on the reconstructed image, and then the reconstructed image can be repeatedly corrected by minimizing the difference between the calculated measurements and the real ones. In this way, the optimization method can be used for collaboration and then the iteration reconstruction algorithm can be developed.

2.2. Structured compressed sensing for PAI

In this paper, including the structured compressed sensing, we build up a novel model for the PAI reconstruction. We define a new variable f as:

$$f(\vec{r}_0, t) = \frac{4\pi C_p}{\mu}\int_0^t p(\vec{r}_0, t')\,\mathrm{d}t' \cdot t \tag{3}$$

where t' is the integration variable.

Then Eq. (2) can be converted as follows:

$$f(\vec{r}_0, t) = \oiint_{|r-r_0|=ct}u(\vec{r})\mathrm{d}^2\vec{r} \tag{4}$$

In practical imaging, the reconstructed image and the measurements are processed discretely, and the image is reshaped into vectors for convenience. If the size of the reconstructed image $u(\vec{r})$ is X pixels $\times$ Y pixels, the total pixel number of the reconstructed image $u(\vec{r})$ is N ($N = XY$). After vectorization, the reconstructed image $u(\vec{r})$ becomes a vector u with the length of N. If the total number of the detection points is Q, the length of measurement in each detection point is M, Eq. (4) can be expressed as:

$$f_i = A_i^\mathrm{T} \cdot u \quad i = 1, 2, \ldots, Q \tag{5}$$

where f_i is the integration of the $u(\vec{r})$ along the arc that is centered in ith detection point and with a radius of ct, A_i is the projection matrix of the ith detection point, T is the transpose operation of a matrix. The calculation of the projection matrix is as follows:

(a) Calculate a matrix $A_i(j)$ as:

$$A_i(j) = \max\left\{1 - \left|\frac{z \cdot \mathrm{d}x}{c \cdot \mathrm{d}t} - j\right|, 0\right\}(1 \le j \le M) \tag{6}$$

where $z = \sqrt{(m - m_i)^2 + (n - n_i)^2}$, (m, n) is the coordinate of the matrix $A_i(j)$, (m_i, n_i) is the position of the ith detection point, $\mathrm{d}x$ is the actual length between two pixels in the reconstructed image, $\mathrm{d}t$ is the discretized time step and M is the total sampling points at one detection point.

(a) $A_i(j)$ is a $N \times M$ matrix. The value of each point (m, n) in the matrix $A_i(j)$ is calculated by Eq. (6).
(b) Vectorize the matrix $A_i(j)$ as the jth column vector in projection matrix A_i.

(c) Repeat the calculation M times to get the projection matrix A_i.

(d) Repeat step (a) to step (c) Q times to get the projection matrix in the different sampling positions $(A_1, A_2, \ldots, A_Q)$.

Then write the projection matrixes in the forms as follows:

$$
A = \begin{pmatrix} A_1^T \\ A_2^T \\ \vdots \\ A_Q^T \end{pmatrix} \tag{7}
$$

Eq. (6) can be expressed as:

$$
f = A \cdot u \tag{8}
$$

where the sizes of f, A and u are MQ pixels $\times 1$ pixel, MQ pixels $\times N$ pixels and N pixels $\times 1$ pixel respectively.

In structured compressed sensing, the vector u can be viewed as a concatenation of K blocks:

$$
u = [\underbrace{u_1, \ldots, u_d}_{u^T[1]}, \underbrace{u_{d+1}, \ldots, u_{2d-1}}_{u^T[2]}, \ldots \underbrace{u_{N-d+1}, \ldots, u_N}_{u^T[K]}] \tag{9}
$$

In this paper, we assume each block has the same length of d elements, and $u[k]$ denotes the kth block.

Generally, to reconstruct the photoacoustic image from incomplete measurements by using the structured compressed sensing theory, we can solve an optimization problem as follows:

$$
\min_u \left\{ |u|_{2,1} + \frac{1}{2} |Au - f|_2^2 \right\} \tag{10}
$$

where $|u|_{2,1} = \sum_{k=1}^K |u[k]|_2$, $|\ |_2$ is the L_2-norm.

2.3. Block-sparse model-based reconstruction algorithm

In this paper, we use the DCT model described in Ref. [42] to process the received signals f first to scale down the dataset. Then we use the block-sparse method for image reconstruction.

The DCT calculation can be processed in the form of matrix multiplication as follows:

$$
F = Df \tag{11}
$$

where D is the DCT matrix and its size is $MQ \times MQ$. The matrix D can be calculated as

$$
D_{xy} = \begin{cases} \dfrac{1}{\sqrt{MQ}} \cos\left(\dfrac{\pi(2x-1)(y-1)}{2MQ}\right) & x = 1 \\[4mm] \sqrt{\dfrac{2}{MQ}} \cos\left(\dfrac{\pi(2x-1)(y-1)}{2MQ}\right) & 2 \le x \le MQ \end{cases} \tag{12}
$$

where x and y are the row and column indexes in the DCT matrix D.

The DCT processed relationship between the signals and the photoacoustic image can be expressed as

$$
F = Gu \tag{13}
$$

where we assuming $G = DA$ for succinct expression.

We set a threshold here and the significant DCT coefficients with relatively major information will be selected to reconstruct the image. After selecting the coefficient, the amount of the dataset is supposed to be reduced. If the threshold is set to be TH, the selection index set can be obtained by

$$
\left\{ a \mid a = 1, 2, 3, \ldots, MQ \quad |F_a| > TH \right\} \tag{14}
$$

The DCT coefficients F are reduced to F_{TH} after the selection, and it can be expressed as

$$
\left\{ F_{TH} \mid a = 1, 2, 3, \ldots, MQ \quad |F_a| > TH \right\} \tag{15}
$$

The measurement matrixes G are modified correspondingly by keeping the rows whose index are in the set (14). Then the reduced measurement matrix, which is denoted by G_{TH}, can be obtained.

After the reduction, the image reconstruction problem can be expressed as

$$
\min_u \left\{ |u|_{2,1} + \frac{1}{2} |G_{TH}u - F_{TH}|_2^2 \right\} \tag{16}
$$

We use a Barzilai–Borwein (BB) [48] to solve this block-sparse problem. The iterative procedure of (16) for one block $u[k]$ is given by

$$
\begin{cases} h = u^q[k] - \mu_k^q G_{TH}^T[k] \left(G_{TH}u^q - F_{TH}\right) \\[3mm] u^{q+1}[k] = \dfrac{h}{|h|_2} \max\left\{ |h|_2 - \mu_k^q \eta, 0 \right\} \end{cases} \tag{17}
$$

where $u^q[k]$ and $u^{q+1}[k]$ are the kth block of the image vector u in qth and $(q+1)$th iteration, μ_k^q is the Barzilai–Borwein step parameter for kth block in qth iteration, $G_{TH}[k]$ is the kth block of the reduced measurement matrix, η is the shrinkage parameter. h is the variables used for a succinct expression. Here, we choose μ_k by BB method for every iteration

$$
\mu_k^{q+1} = G_{TH}^T[k]G_{TH} \left(u^{q+1} - u^q\right) \tag{18}
$$

where μ_k^q is the Barzilai–Borwein step parameter for kth block in $(q+1)$th iteration.

As a result, the BS-DCT algorithm is summarized as follows:

1. Initialization: input η, μ_0, TH and K. Set the reconstructed image $u^0 = 0$, $q = 0$.
2. Calculate the selection index set by (14). According to the selection index set, get the reduced measurement matrix G_{TH}.
3. For $k = 1,2,3,\ldots,K$, compute $u^q[k]$ by Eq. (17) and update the u^q.
4. Update μ_k^q using Eq. (18).
5. Terminate the iteration when the exiting condition is met. Otherwise repeat the step from (2) to (3). The exiting condition is as follows:

$$
\frac{\|u^q - u^{q-1}\|}{\|u^q\|} < \varepsilon \tag{19}
$$

3. Simulation

In this section, we present numerical results to illustrate the effectiveness of the proposed BS-DCT algorithm on PAI reconstructions. We compare BS-DCT with the state-of-the-art algorithms like the FBP, the DCT model-based and the TV-GD algorithms. All the simulations are made by using Matlab v7.14 on a PC with Intel Xeon processor and 32 GB memory. The sound speed is set to be consistent as 1540 m/s during the simulation.

3.1. Selection of the threshold and the number of blocks

In the simulation, we choose the vessel phantom with different optical absorption density as the initial pressure rise distribution. The phantom is shown in Fig. 1. The size of the phantom is 89.6 mm $\times$ 89.6 mm, the radius of the scanning circle is 45 mm and the size of the reconstructed image is 128 pixel $\times$ 128 pixel. The scanning step of tomographic angels is set to 9° with 40 tomographic views covers the full 360° of the scanning plane. The photoacoustic signals are generated by Eq. (2).

Fig. 1. The given optical absorption distribution image.

As mentioned before, the choice of threshold TH plays a critical role in the reconstruction performance. By setting the threshold TH to be 0.01, 0.02, 0.04 and 0.06 with a fixed blocks number of 16, the images are reconstructed respectively. The numbers of the iterations are all set to be 10. The reconstruction results are shown in Fig. 2.

The result shows that there is a trade-off between the reconstruction quality and the computation reduction through the choice of threshold TH. The smaller TH is, the bigger the dataset scale is and more computational cost it will demand. It is shown in Fig. 2 that the reconstruction results with a threshold of 0.01 and 0.02

are highly close to the original optical absorption distribution. As the TH increases, the reconstructions have a decline in image quality visually. The vessel part of the phantom is severely blurred and there is some noise in the background.

To evaluate the block division's influence to the reconstruction quality, we divide the image vector into 8, 16, 64 and 256 blocks and reconstruct the image under all four threshold conditions mentioned above. We calculate the mean-square error (MSE) of the reconstruction result with the original vessel phantom as standard to evaluate the effect of blocks number K to the reconstruction quality. The DCT model-based algorithm in Ref. [42] is also an efficient iterative algorithm with different threshold, so here we choose it as a comparison with the BS-DCT algorithm. The quantitative result is shown in Fig. 3.

Fig. 3 shows how the MSE curves of DCT, 8-blocks, 16-blocks, 64-blocks and 256-blocks change respectively, along the increasing number of threshold TH. It is seen that the MSE curves of the BS-DCT with different block divisions keep lower level than the DCT model-based algorithms and 8-blocks MSE curve keeps the lowest level among these setups. The more blocks divided, the more nonzero blocks appear and the image is more difficult to recover. But when the blocks division keeps decreasing, it appears that the number of nonzero blocks in 8-blocks and 16-blocks are similar. So the quality of the reconstruction stops improving. Also from the quantitative results, we can confirm that the reconstruction quality declines as the threshold TH increases.

As the discussion note above, we set the threshold TH to be 0.04 and the block division to be 16 in the later simulations as this setup can balance the reconstruction quality and computational efficiency appropriately.

As the threshold and the block division setup are determined, we compare the proposed algorithms with the state-of-the-art algorithms, the FBP [18], the TV-GD [38], the wavelet packets
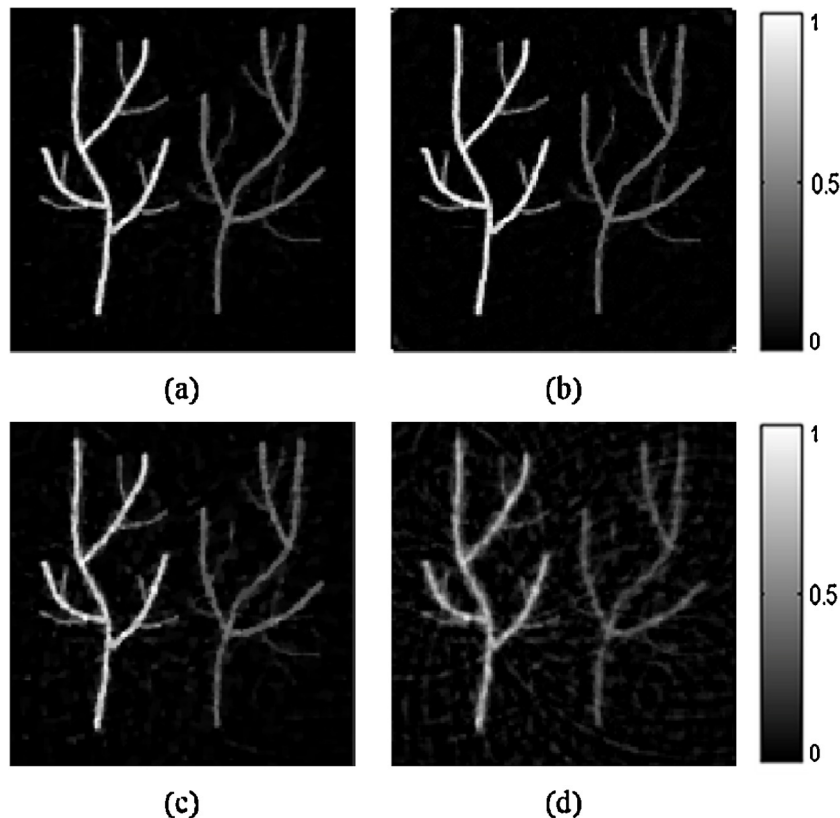

Fig. 2. The simulation result of the BS-DCT reconstruction algorithm with different thresholds TH: (a) 0.01 (b) 0.02, (c) 0.04 and (d) 0.06.
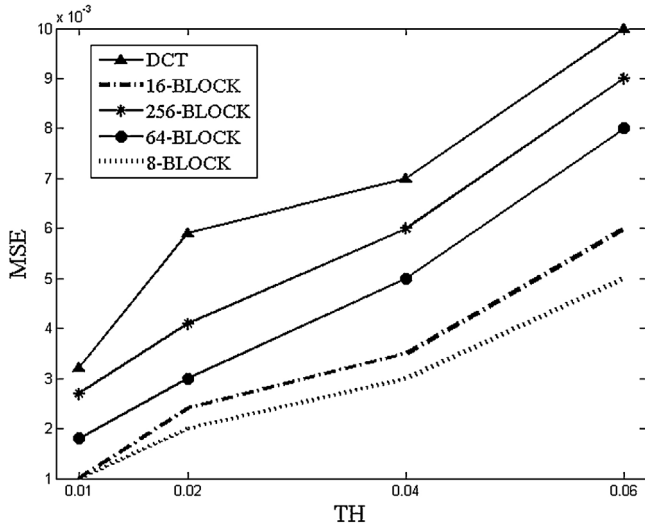
Fig. 3. The quantitative analysis of the DCT model-based reconstruction algorithm and the BS-DCT algorithm with different block division.

model-based [32] and the DCT model-based algorithms [42]. The reconstruction results are shown in Fig. 4. We use the shep-logan phantom here as the original optical absorption distribution to compare the proposed BS-DCT algorithm with the other state-of-the-art algorithms in reconstructing a complex structured imaging object. It's worthwhile to note that the simulation setups used in the TV-GD algorithm, wavelet model-based and DCT-based algorithm are the appropriate setups reported in Refs. [38,32,42], respectively.

It is shown in Fig. 4 that all four iterative algorithms have comparable reconstruction results through the eye test. The contrast of the FBP reconstruction is not as high as the other three. When the sampling point gets sparse in the FBP reconstruction, the arc-like artifacts appears due to the back-projection arcs cannot be canceled out with each other. It is safe to say that the FBP algorithm is not applicative in this sparse-sampling view condition. The iterative algorithms can provide better qualities of

the reconstructed images than the FBP method in sparse-view reconstructions.

Also, we include a line-plots image of the reconstruction result by the TV-GD algorithm, the wavelet model-based algorithm, the DCT model-based algorithm and the proposed BS-DCT algorithm to show the details of the iterative reconstruction results clearly. The location of the pixel profile in the image is displayed in Fig. 5(a). The comparisons of pixel profiles are displayed in Fig. 5(b).

In Fig. 5(b), the solid line, the dash-dotted line, the dashed line and the dotted line represent the pixel profiles of the TV-GD, the wavelet model-based, the DCT model-based and the BS-DCT image respectively. It is shown in Fig. 5(b) that all the iterative algorithms can reconstruct the image precisely. Between DCT model-based algorithms and BS-DCT algorithms, we show the pixel profiles of those two in Fig. 5(c). The dotted and solid lines represent the pixel profiles of the DCT model-based and the BS-DCT image respectively. It is shown in Fig. 5(c) that the DCT model-based algorithm image has some impulse noise in the edge area and is not able to suppress the noise in the flat area. The profiles of the BS-DCT image match with the original one more precisely.

We also explore the influence of different scanning views to iterative image reconstruction. Four different measurements are collected. The scanning step of tomographic angels is set to 2.25°, 4°, 9° and 12° respectively. So the sampling points are 160 views, 90 views, 40 views and 30 views correspondingly. We calculate the peak signal-to-noise ratios (PSNR) of reconstructed images to evaluate the quality of reconstruction. The PSNR value and computational time of the reconstruction results are listed in Table 1.

From Table 1, it is shown that the PSNR of the FBP algorithm is always at a very low level due to its unsuitability for sparse-view sampling condition. The rest three iterative can maintain good reconstruction quality through the reduction of scanning angles. As for the computational time, the iterative algorithms are basically proportional to the number of scanning angles. But with more sufficient data, they can meet the exit condition with less amount of iterations.

In this part, the BS-DCT algorithm is proved to be accurate and stable for practical PAI image reconstruction.
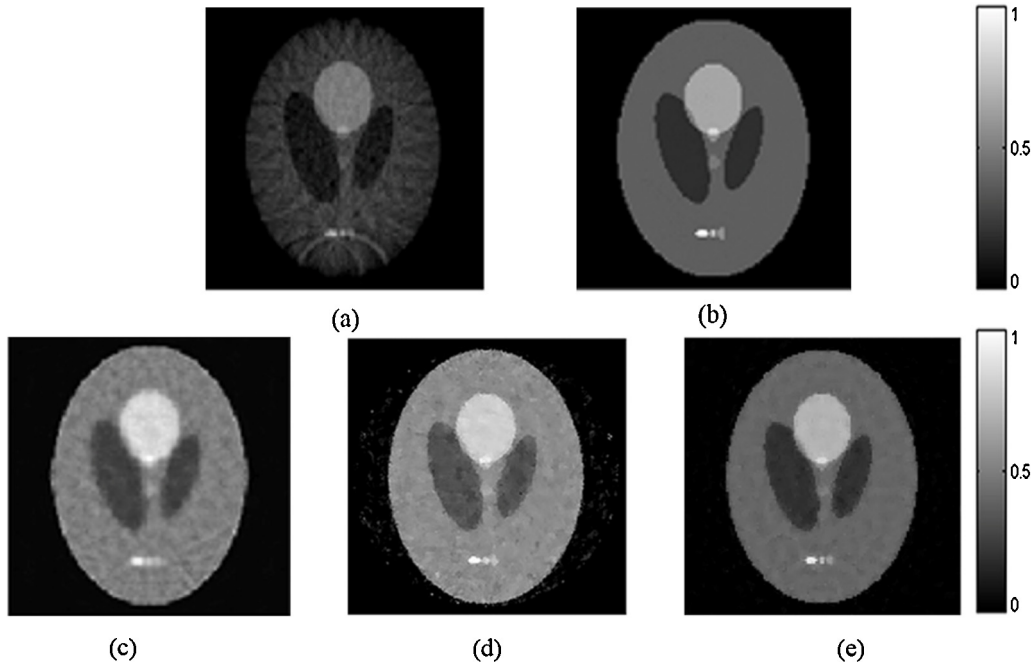

Fig. 4. The reconstructed images with (a) the FBP algorithm, (b) the TV-GD algorithm, (c) the wavelet model-based algorithm, (d) the DCT model-based algorithm and (e) the BS-DCT algorithm.
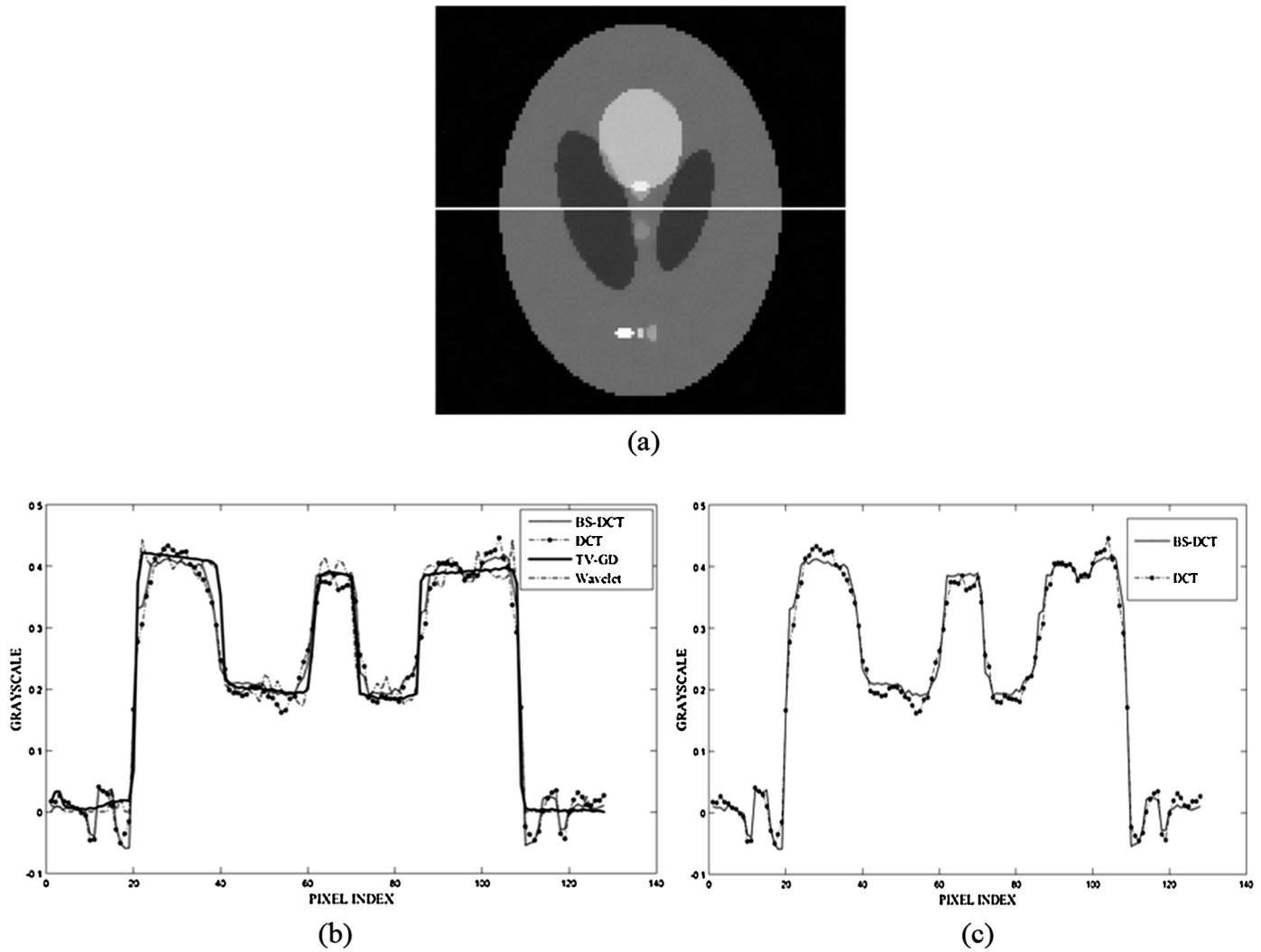
(a)

(b)

(c)

Fig. 5. The line profile of the reconstructed images by the TV-GD algorithm, the DCT model-based algorithm, the wavelet model-based algorithm and the BS-DCT algorithm, respectively.

3.2. Computational efficiency

There are three essential factors in computational efficiency of the PAI reconstruction: the calculation complexity, the number of iterations and the algorithm implementation.

For the calculation complexity part, the involving of DCT into the PAI reconstruction can significantly scale down the data and calculation complexity as discussed in Ref. [42]. During the reconstruction, the original length of the DCT coefficients is MQ. The length of DCT coefficients can be reduced to εMQ ($0 < \varepsilon < 1$). The scale of the measurement matrix G_{TH} reduced to εNMQ. In step 2, the calculation of vector f and the DCT processing require $2O(M^3)$ operations. In step 3, the calculation complexity during one iteration is $O[N(\varepsilon M)^2 + N^2 \varepsilon MQ]$. In step 4, the update of μ_k^q can use the result from step 3. There are no extra operations needed. Here we supposed the iteration is lasted N_{iter} times,

the calculation complexity of the image reconstruction process is $O[2 M^3 + N_{iter} N(\varepsilon M)^2 + N_{iter} N^2 \varepsilon MQ]$. The calculation complexity of the state-of-the-art iterative reconstruction algorithm (e.g., TV-GD algorithm) is $O[M^3 + N_{iter} NM^2 + N_{iter} N^2 MQ]$. In practical image reconstruction, the first two terms are much smaller than the last one, so the calculation complexity of the reconstruction algorithm is determined by the last term. As the other parameters are the same between those two algorithms, the calculation is decided by the reduction ratio ε. From the simulation results in Section 3.1, if threshold TH is set to be 0.04, the value of ε can be 0.1. The calculation complexity is reduced to about 10% of the state-of-the-art iterative reconstruction algorithm calculation complexity. The simulation results in Section 3.1 also indicate that the proposed BS-DCT method hold a smaller reduction ratio ε for accurate image reconstruction than the DCT model-based one in Ref. [42]. As for the wavelet model-based algorithm in Ref. [32],

Table 1
PSNR and computational time of the reconstruction from different scanning views.

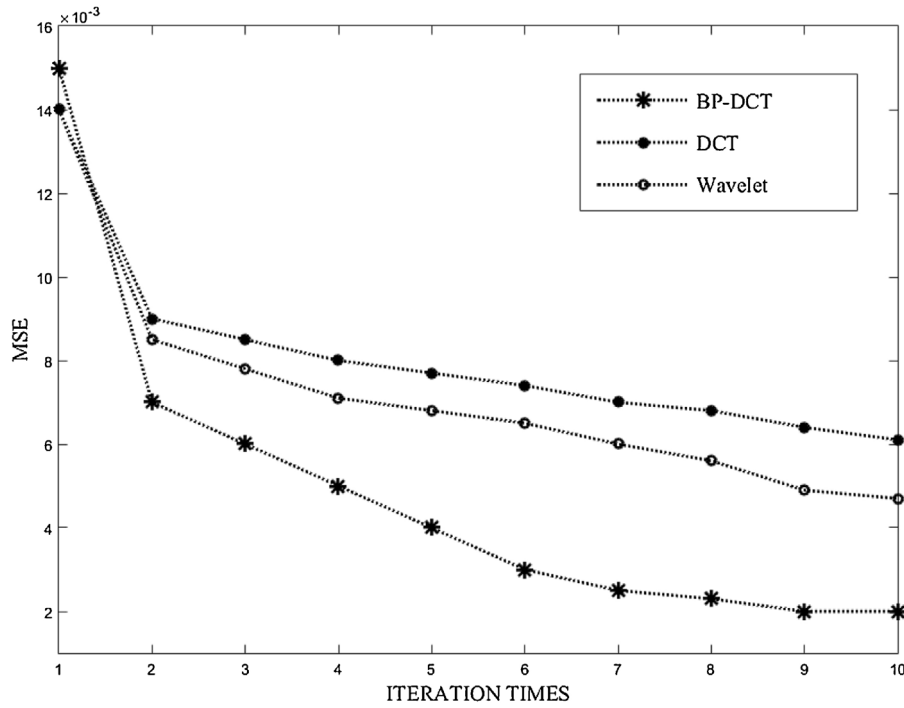| PSNR(dB)/time(s)	TV-GD	DCT model-based	Wavelet model-based	BS-DCT
160-views	38.01/1321.3	31.73/210.2	31.23/251.2	34.02/44.1
90-views	38.23/839.1	30.17/133.5	31.27/181.3	33.18/22.3
40-views	37.81/368.0	28.12/67.3	27.87/92.4	32.12/12.5
30-views	36.68/283.1	27.86/50.2	26.12/44.2	30.93/8.7

Fig. 6. The MSE between the reconstructed images and the original phantom image *versus* the iteration times.

it uses the wavelet-packet base for choosing the 'significant' signal rows with a compression ratio ε'. During each iteration, the calculation complexity is $O[N^2 + N^2\varepsilon MQ]$. It is slightly bigger than the BS-DCT complexity which is $O[N(\varepsilon M)^2 + N^2\varepsilon MQ]$. But before the iteration, the wavelet decomposition is required. The complexity cost of the decomposition is $O[4INMQ + N^3MQ + IN^2MQ]$ where I represents the wavelet decomposition level. As a result, the complexity of the wavelet model-based algorithm is much bigger than the proposed BS-DCT algorithm.

We adopted the Barzilai–Borwein step size selection method to the BS-DCT algorithm. Theoretically, it can improve the convergence speed significantly and reduce the number of iterations. We use the DCT model-based algorithm as a comparison. For the quantitative analysis, we use the MSE between the reconstructed image and the original phantom image to show the improvement of the image quality in every iteration step. The simulation condition is remaining the same with Section 3.1. Each algorithm run the iteration for 10 times. The result is shown in Fig. 6. The line '-', the line '0 -' and the line '*-' represent the DCT model-based, the wavelet model-based and the BS-DCT algorithms, respectively. The images reconstructed by the BS-DCT algorithm in each iteration have smaller value of MSE than the wavelet and DCT ones. If we set the MSE value of 0.007 as a requirement, the BS-DCT algorithm can meet the request 6 iteration step ahead of the other two.

From the description in Section 2.3, the proposed BS-DCT algorithm updates the reconstruction through Eq. (17) in each iteration. A closer look at Eq. (17) will find that only the information within each block is needed when the reconstruction is updated block by block as the term $(G_{TH}u^q - F_{TH})$ in Eq. (17) can be calculated outside the whole block updating process. Due to this block independent nature, the CPU-based parallel calculation implementations can be adopted to make single iteration faster. We compare the computational times of the single iteration of the DCT model-based, the wavelet model-based, the BS-DCT without parallelization strategies and the BS-DCT with parallelization. The size of the reconstructed image is 128 pixel × 128 pixel,

256 pixel × 256 pixel, and 512 pixel × 512 pixel. The result is shown in Table 2. The paralleled single iteration time cost is 0.6 s, more than 10 times faster compared to the DCT model-based one of 8.3 s.

In this part, we investigated the computational efficiency of our proposed algorithm in the calculation complexity, the number of iterations and algorithm implementation. It can be surmised that the proposed BS-DCT algorithm has the advantage in computational efficiency.

3.3. Limited-view and sparse-view sampling simulation

In the practical application of the PAI, the full angular scanning condition can hardly be achieved. Through the simulation under the limited-view condition and line-view condition, we evaluate the performance of the proposed BS-DCT algorithm practically.

The simulation setup and the reconstructed image is shown in Fig. 7. In the limited-view simulation as shown in Fig. 7(a), the scanning angular range is set to 150° and the angular step is 3°, so 50-view photoacoustic signals are obtained. In the line-view simulation as shown in Fig. 7(c), the transducer array with 60 transducers is placed in the right side of the imaging object and the interval between two transducer elements is 1.49 mm. It is revealed in Fig. 7(b) and (d) that the quality of the BS-DCT reconstruction survived from the limitation of the sampling angle. However, there are some information missing under this sampling condition, yet the BS-DCT method can still provide a satisfying reconstruction.

Table 2
Computational times of the image reconstruction by the use of different algorithms (second/iteration).

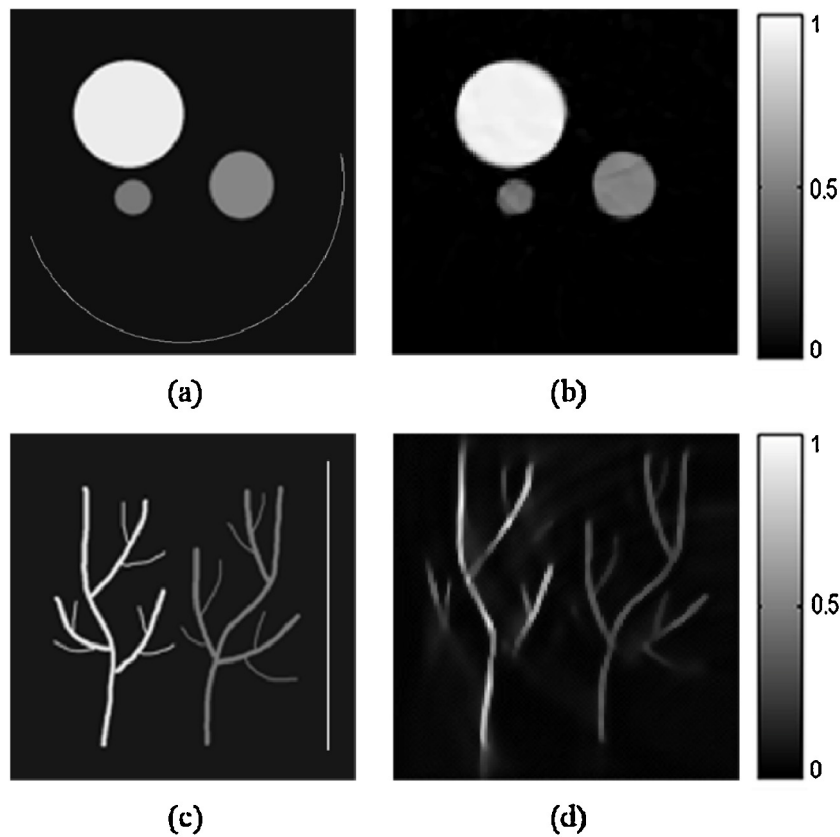| Image size	DCT	Wavelet	BS-DCT	BS-DCT (parallelization)
128 pixel × 128 pixel	8.3	10.6	3.2	0.6
256 pixel × 256 pixels	33.7	42.7	11.8	1.9
512 pixel × 512 pixel	138.2	156.1	48.2	8.3

Fig. 7. Limited-view image reconstruction and line-view image reconstruction. (a) Refers to the location of transducers in the limited-view simulation. (b) Refers to the reconstructed image from the limited-view data. (c) Refers to the location of transducers. (d) Refers to the reconstructed image from the line-view data.

3.4. Robustness to noise

In the practical applications of the PAI, the signal acquisition progress is usually polluted by measuring noises from the ultrasound transducers and system electronics. An algorithm with practical potential is expected to maintain stability in the noisy circumstance. In the practical applications, the robustness is a crucial factor to evaluate algorithms other than the computational cost and reconstruction quality. To analyze the robustness of the proposed BS-DCT algorithm, white Gaussian noises of different power levels are added to the simulated photoacoustic signals. The signal-to-noise ratio (SNR) of the polluted photoacoustic signals is 10 dB, 5 dB and 3 dB respectively. The reconstruction results are shown in Fig. 8.

It is shown in Fig. 8 that with the SNR level of 10 dB and 5 dB, the reconstructed image has hardly any difference with the reconstruction result from the noise-free photoacoustic signals. The noise suppression is effective and the details in the reconstructed images are well preserved. As the noise gets stronger, the quality of reconstruction declines and there is some pulse noise in the background. But the main structure of the phantom still remain clear.

In this section, the robustness of the proposed BS-DCT algorithm is evaluated. The results demonstrate that the proposed algorithm stay stable and functional under the SNR level of the photoacoustic signals is greater than 3 dB, which is close to the practical application circumstance.

4. *In vitro* experiments

4.1. Experiment setup

We also verified the BS-DCT algorithm through *in-vitro* experiment to demonstrate its performance in the practical PAI application. Fig. 9(a) illustrates the PAI platform we used to carry out the experiment. The laser pulse is emitted by a Nd:YaG laser generator (Continum, Surelite I) with the wavelength of 532 nm. The single laser pulse is generated with a repetition rate of 10 Hz and last 6-7 ns. The incident laser pulse is emitted toward the top of the phantom through a concave lens (its diameter: 5 cm). The setup of lens enlarges the illuminations area and keep the pulse energy of 6.47 mJ/cm^2 in the illumination area lower than the ANSI laser radiation safety standard (20 mJ/cm^2) [1]. The transducer we used to receive the photoacoustic signals is a linearly unfocused on with a central frequency of 3.5 MHz (−6 dB bandwidth at 45%). A digital stepping motor (GCD-0301M) is used to rotate the transducer around the phantom placed in water with a scanning radius of 38 mm. The acquired photoacoustic signals are amplified by a pulse receiver (Panametric, 5900PR). An oscilloscope (Agilent, 54622D) with a sampling frequency of 16.67 MHz is applied to transform the acquired photoacoustic signals into digital ones. The whole system is controlled by a computer through the serial interface. The transformed digital data is transported to the computer through the general purpose interface bus (GPIB) and processed on the computer.

The imaged phantom we used in the experiment is made by gelatin cylinder. It is shown in Fig. 9(b) and (c). There are two different phantoms. The radius of the phantom is 25 mm. The left one is made by three rubber bars with 1 mm diameter that embedded as the optical absorbers. The right one utilizes leaf which pretends as vein and tissue as the optical absorbers.

It's also worth to note that during the experiment, the transducer tends to measure the photoacoustic signal in-plane only, and the reconstruction is also in 2D. The angular step of sampling is set as 9°, and the photoacoustic signals at 40 sampling positions can be acquired. The cross-sectional image in any plane is mainly
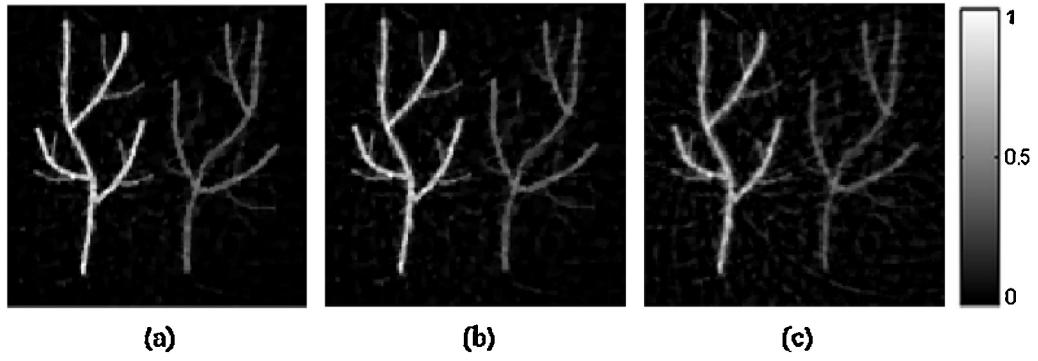
Fig. 8. The BS-DCT reconstruction results from noisy data with the SNR of (a) 10 dB, (b) 5 dB, and (c) 3 dB, respectively.

determined by the measured data in the same plane, and a set of circular measurement data on the same plane would be sufficient to reconstruct a good image. We use the de-convolution calculation before the reconstruction to eliminate the transducer's impulse response influence.

Through the numerical simulation, the DCT model-based is closest to the proposed algorithm in computational time and calculation complexity and TV-GD is reported as a stable and practical iterative algorithm in photoacoustic imaging. So here we select them to be comparison with the proposed BS-DCT algorithm.

4.2. Experiment result

The images are constructed by the FBP, the TV-GD, the DCT model-based and the BS-DCT algorithms, respectively. The reconstruction results are shown in Fig. 10.
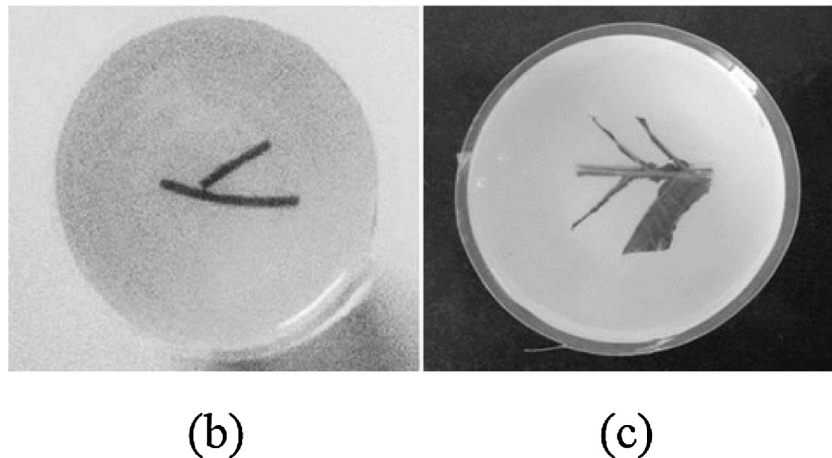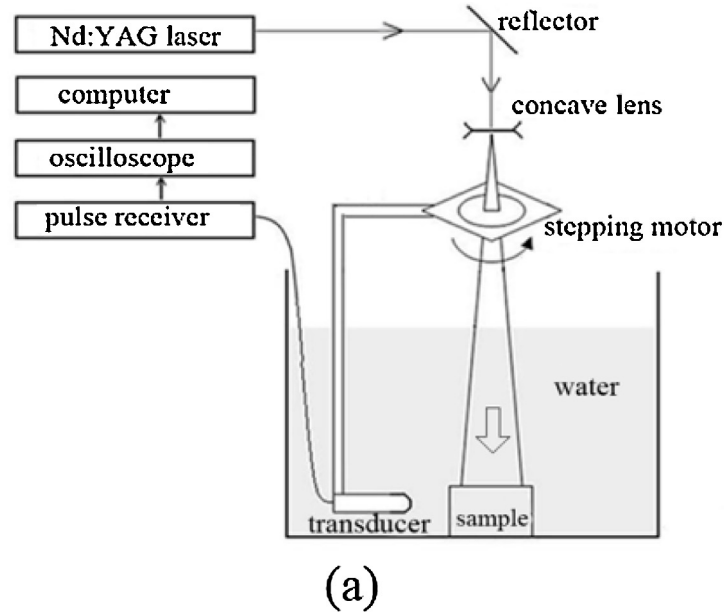

Fig. 9. (a) The scheme of the experiment platform. (b) The photo of the imaging samples. (c) The photo of leaf samples.
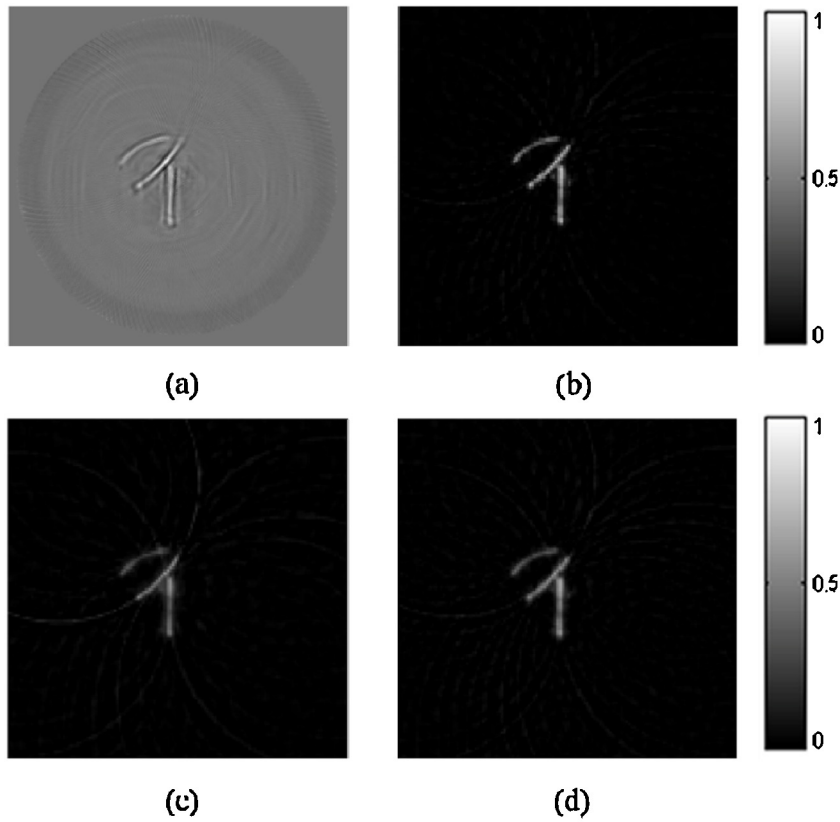
Fig. 10. Reconstructed images of rubber sample by (a) the FBP, (b) the TV-GD, (c) the DCT model-based, and (d) the BS-DCT algorithms, respectively.
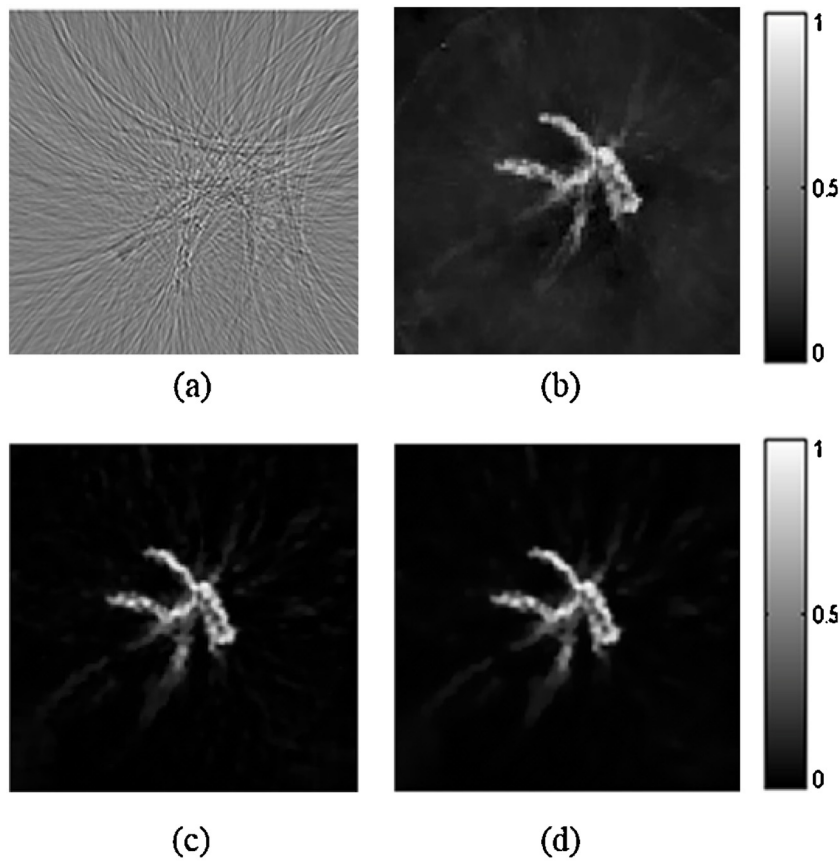

Fig. 11. Reconstructed images of leaf sample by (a) the FBP, (b) the TV-GD, (c) the DCT model-based, and (d) the BS-DCT algorithms, respectively.

It is shown in Fig. 10 that the FBP reconstruction is strongly affected by the artifacts and noise in the background. The main structure of the phantom is seriously blurred. All three iterative algorithms can provide high-contrast images with less noise. The BS-DCT reconstruction outperforms the DCT model-based algorithm in the image contrast and noise suppression. The BS-DCT reconstruction quality is really close to the TV-GD reconstruction as the structure of the phantom is clear and the noise in the background is well-suppressed.

In vitro imaging of a leaf vein is also performed to further demonstrate the quality of the BS-DCT algorithm. The reconstruction result is shown in Fig. 11. As the structure of the phantom is more complex, the FBP are deeply influenced by the artifact and fail to reconstruct the accurate image. It is shown in the image reconstructed by the proposed BS-DCT algorithm that the edges of the optical absorbers are quite easy to recognize. Fewer artifacts and noises are shown in the background of the reconstructed image. This may contribute to better application in clinical analysis.

From the experiment result noted above, it is safe to say that the BS-DCT algorithm would provide stable and accurate reconstruction with much improved computational efficiency in the practical PAI application.

5. Conclusion

In order to accelerate the PAI reconstruction and reduce its computational cost, we propose the BS-DCT algorithm that adopts the structured compressed sensing theory to the PAI for the first time. First, we adopt the DCT to eliminate the minor coefficients and reduce the data scale. After scaling down the dataset, a block-sparse based iterative method is proposed to accomplish the image reconstruction. Due to its block independent nature, we use the CPU-based parallel calculation implementation to accelerate the reconstruction. Our implementation of the BS-DCT algorithm improved the computational efficiency over 10 times compared to the original DCT model-based algorithm. During the iterative reconstruction, the number of iterations required is reduced by adopting the fast-converging optimization Barzilai–Borwein method. The numerical simulations and *in-vitro* experiments are carried out and the results are presented. The results show that the reconstruction quality is in the same level with the state-of-the-art iterative algorithms such as the TV-GD algorithm and the DCT model-based algorithm. Our algorithm requires less number of iterations with a reduced data scale and significantly accelerated through parallel calculation implementation.

It is also worth to mention that the GPU-based parallel photoacoustic algorithm in Ref. [41] focuses on using parallelization strategies to accelerate the existing image reconstruction algorithms. The parallelization strategies by use of GPUs are of general interest. Almost every iterative image reconstruction algorithm has a similar pair of projection/back-projection operations. The proposed parallelization strategies in Ref. [41] can also be used to implementing the proposed BS-DCT algorithm on GPU. During the GPU implementations, the measurement data scale and convergence speed are two aspects that can be further improved through developing advanced image reconstruction algorithms. Through the discussion above, the proposed BS-DCT algorithm requires less amount of measurement data for accurate image reconstruction and is a fast-converging optimization algorithms that requires less iterations for convergence. Implementing the BS-DCT algorithm on GPU can continue improving the computational efficiency of the photoacoustic image reconstruction.

In conclusion, the BS-DCT algorithm may be an effectively accelerated practical algorithm for PAI reconstruction.

References

[1] Lihong V. Wang, Tutorial on photoacoustic microscopy and computed tomography, IEEE J. Sel. Top. Quantum Electron. 14 (1) (2008) 171–179.
[2] Minghua Xu, Lihong V. Wang, Photoacoustic imaging in biomedicine, Rev. Sci. Instrum. 77 (4) (2006) 041101.
[3] Changhui Li, Lihong V. Wang, Photoacoustic tomography and sensing in biomedicine, Phys. Med. Biol. 54 (19) (2009) R59.
[4] Lihong V. Wang, Prospects of photoacoustic tomography, Med. Phys. 35 (12) (2008) 5758–5767.
[5] Robert A. Kruger, Daniel R. Reinecke, Gabe A. Kruger, Thermoacoustic computed tomography–technical considerations, Med. Phys. 26 (9) (1999) 1832–1837.
[6] Robert A. Kruger, Pingyu Liu, Robert C. Appledorn, Photoacoustic ultrasound (PAUS)-reconstruction tomography, Med. Phys. 22 (10) (1995) 1605–1609.
[7] Xueding Wang, et al., Noninvasive laser-induced photoacoustic tomography for structural and functional in vivo imaging of the brain, Nat. Biotechnol. 21 (7) (2003) 803–806.
[8] Hao F. Zhang, et al., Functional photoacoustic microscopy for high-resolution and noninvasive in vivo imaging, Nat. Biotechnol. 24 (7) (2006) 848–851.
[9] Li Li, et al., Photoacoustic imaging of lacZ gene expression in vivo, J. Biomed. Opt. 12 (2) (2007), 020504(1)-020504(3).
[10] Bin Guo, et al., Multifrequency microwave-induced thermal acoustic imaging for breast cancer detection, IEEE Trans. Biomed. Eng. 54 (11) (2007) 2000–2010.
[11] Manojit Pramanik, et al., Design and evaluation of a novel breast cancer detection system combining both thermoacoustic (TA) and photoacoustic (PA) tomography, Med. Phys. 35 (6) (2008) 2218–2223.
[12] Adam de La Zerda, et al., Photoacoustic ocular imaging, Opt. Lett. 35 (3) (2010) 270–272.
[13] E.Z. Zhang, et al., In vivo high-resolution 3D photoacoustic imaging of superficial vascular anatomy, Phys. Med. Biol. 54 (4) (2009) 1035.
[14] Joël J. Niederhauser, et al., Combined ultrasound and optoacoustic system for real-time high-contrast vascular imaging in vivo, IEEE Trans. Med. Imaging 24 (4) (2005) 436–440.
[15] Jan Laufer, et al., Quantitative spatially resolved measurement of tissue chromophore concentrations using photoacoustic spectroscopy: application to the measurement of blood oxygenation and haemoglobin concentration, Phys. Med. Biol. 52 (1) (2007) 141.
[16] Adam De La Zerda, et al., Carbon nanotubes as photoacoustic molecular imaging agents in living mice, Nat. Nanotechnol. 3 (9) (2008) 557–562.
[17] Minghua Xu, Lihong V. Wang, Pulsed-microwave-induced thermoacoustic tomography: filtered backprojection in a circular measurement configuration, Med. Phys. 29 (8) (2002) 1661–1669.
[18] Minghua Xu, Lihong V. Wang, Universal Back-projection Algorithm for Photoacoustic Computed Tomography. Biomedical Optics 2005, International Society for Optics and Photonics, San Jose, CA, 2005.
[19] Minghua Xu, Lihong V. Wang, Time-domain reconstruction for thermoacoustic tomography in a spherical geometry, IEEE Trans. Med. Imaging 21 (7) (2002) 814–822.
[20] Minghua Xu, Yuan Xu, Lihong V. Wang, Time-domain reconstruction algorithms and numerical simulations for thermoacoustic tomography in various geometries, IEEE Trans. Biomed. Eng. 50 (9) (2003) 1086–1099.
[21] Yuan Xu, Dazi Feng, Lihong V. Wang, Exact frequency-domain reconstruction for thermoacoustic tomography. I. Planar geometry, IEEE Trans. Med. Imaging 21 (7) (2002) 823–828.
[22] Yuan Xu, Minghua Xu, Lihong V. Wang, Exact frequency-domain reconstruction for thermoacoustic tomography. II. Cylindrical geometry, IEEE Trans. Med. Imaging 21 (7) (2002) 829–833.
[23] Pouyan Mohajerani, Stephan Kellnberger, Vasilis Ntziachristos, Fast fourier backprojection for frequency-domain optoacoustic tomography, Opt. Lett. 39 (18) (2014) 5455–5458.
[24] Chi Zhang, Yuanyuan Wang, Deconvolution reconstruction of full-view and limited-view photoacoustic tomography: a simulation study, J. Opt. Soc. Am. A: Opt. Image Sci. Vis. 25 (10) (2008) 2436–2443.
[25] Chi Zhang, Changhui Li, Lihong V. Wang, Fast and robust deconvolution-based image reconstruction for photoacoustic tomography in circular geometry: experimental validation, IEEE Photonics J. 2 (1) (2010) 57–66.
[26] X. Luís Dean-Ben, Vasilis Ntziachristos, Daniel Razansky, Acceleration of optoacoustic model-based reconstruction using angular image discretization, IEEE Trans. Med. Imaging 31 (5) (2012) 1154–1162.
[27] X. Luís Deán-Ben, et al., Accurate model-based reconstruction algorithm for three-dimensional optoacoustic tomography, IEEE Trans. Med. Imaging 31 (10) (2012) 1922–1928.
[28] Andreas Buehler, et al., Model-based optoacoustic inversions with incomplete projection data, Med. Phys. 38 (3) (2011) 1694–1704.
[29] Calvin B. Shaw, et al., Least squares QR-based decomposition provides an efficient way of computing optimal regularization parameter in photoacoustic tomography, J. Biomed. Opt. 18 (8) (2013), 080501(1)-080501(3).

[30] Jean Provost, Frederic Lesage, The application of compressed sensing for photo-acoustic tomography, IEEE Trans. Med. Imaging 28 (4) (2009) 585–594.

[31] Zijian Guo, et al., Compressed sensing in photoacoustic tomography in vivo, J. Biomed. Opt. 15 (2) (2010), 021311(1)-021311(6).

[32] Amir Rosenthal, et al., Efficient framework for model-based tomographic image reconstruction using wavelet packets, IEEE Trans. Med. Imaging 31 (7) (2012) 1346–1357.

[33] Jing Meng, et al., Compressed-sensing photoacoustic computed tomography in vivo with partially known support, Opt. Express 20 (15) (2012) 16510–16523.

[34] Jing Meng, et al., In vivo optical-resolution photoacoustic computed tomography with compressed sensing, Opt. Lett. 37 (22) (2012) 4573–4575.

[35] Lei Yao, Huabei Jiang, Photoacoustic image reconstruction from few-detector and limited-angle data, Biomed. Opt. Express 2 (9) (2011) 2649–2654.

[36] Lei Yao, Huabei Jiang, Enhancing finite element-based photoacoustic tomography using total variation minimization, Appl. Opt. 50 (25) (2011) 5031–5041.

[37] Kun Wang, et al., Investigation of iterative image reconstruction in three-dimensional optoacoustic tomography, Phys. Med. Biol. 57 (17) (2012) 5399.

[38] Yan Zhang, Yuanyuan Wang, Chen Zhang, Total variation based gradient descent algorithm for sparse-view photoacoustic image reconstruction, Ultra-sonics 52 (8) (2012) 1046–1055.

[39] Chen Zhang, Yan Zhang, Yuanyuan Wang, A photoacoustic image reconstruction method using total variation and nonconvex optimization, Biomed. Eng. Online 13 (1) (2014) 117.

[40] Chen Zhang, Yuanyuan Wang, High total variation-based method for sparse-view photoacoustic reconstruction, Chin. Opt. Lett. 12 (11) (2014) 111703.

[41] Kun Wang, et al., Accelerating image reconstruction in three-dimensional optoacoustic tomography on graphics processing units, Med. Phys. 40 (2) (2013) 023301.

[42] Yan Zhang, Yuanyuan Wang, Chen Zhang, Efficient discrete cosine transform model–based algorithm for photoacoustic image reconstruction, J. Biomed. Opt. 18 (6) (2013), 066008(1)-066008(9).

[43] Marco F. Duarte, Yonina C. Eldar, Structured compressed sensing: from theory to applications, IEEE Trans. Signal Process. 59 (9) (2011) 4053–4085.

[44] Yonina C. Eldar, Patrick Kuppinger, Helmut Bolcskei, Block-sparse signals: uncertainty relations and efficient recovery, IEEE Trans. Signal Process. 58 (6) (2010) 3042–3054.

[45] Mishali Moshe, Yonina C. Eldar, Blind multiband signal reconstruction: compressed sensing for analog signals, IEEE Trans. Signal Process. 57 (3) (2009) 993–1009.

[46] Jie Chen, Huo. Xiaoming, Theoretical results on sparse representations of multiple-measurement vectors, IEEE Trans. Signal Process. 54 (12) (2006) 4634–4643.

[47] Yuli Fu, Jian Zou, Qiheng Zhang, Li. Haifeng, Recoverability analysis of block-sparse representation, J. Syst. Eng. Electron. 25 (3) (2014) 373–379.

[48] Jonathan Barzilai, J.M. Borwein, Two-point step size gradient methods, Ima J. Numer. Anal. 8 (1) (1988) 141–148.